

DEVELOPMENT OF A LOW ACTUATION VOLTAGE RF MEMS SWITCH

K. S. KIANG¹, H. M. H. CHONG¹, C. J. HWANG², L. B. LOK², K. ELGAID² and M. KRAFT¹

¹Nano Group, School of Electronics and Computer Science,
University of Southampton, Highfield, Southampton, Hampshire, SO17 1BJ United Kingdom

²Ultrafast Systems Group, Department of Electronics and Electrical Engineering,
University of Glasgow, Rankine Building, Oakfield Avenue, Glasgow, G12 8LT United Kingdom

*Corresponding author: K. S. Kiang, Phone: +44 2380 593127, e-mail: ksk05r@ecs.soton.ac.uk

Abstract: This paper reports on the design of a novel ultra low actuation voltage, low loss radio frequency micro-electro-mechanical system (RF MEMS) capacitive shunt switch. The concept of the switch relies on a mechanically unconstrained armature actuated over a coplanar waveguide using electrostatic forces. The minimum actuation voltage of the switch is <2V, with an isolation of 40dB and insertion loss <0.7dB at 78GHz.

Keywords: Low Loss Switch, Low actuation voltage, Electrostatic actuation

INTRODUCTION

RF MEMS switches offer two distinct advantages in comparison with p-i-n diodes and field effect transistors: enhanced RF performances and almost zero power consumption. However, a major disadvantage is the high operating voltage that is required to actuate the switch. A typical MEMS switch requires between 20V-80V for operation [1].

A large variation of MEMS switches were studied and developed by many different research groups [1-3]. The MEMS switch typically use actuation mechanisms such as electrostatic, thermal and piezoelectric, but recently hybrid actuation mechanism, such as magneto-static [4] and thermal-electrostatic [5] were investigated. Many of these studies were conducted with the aim to reduce the actuation voltage of the switch. Several authors [6-7], reported reduced actuation voltage using a serpentine folded suspension. Peroulis [6], achieved a reduction of 80% in the actuation voltage of his switch by increasing the number of meanders of the spring from 1 to 5. However, these structures are complex in design.

This paper presents an extended study and the fabrication process of the design of the spring-less capacitive RF MEMS switch; the concept of which was first described in [8].

MECHANICAL MODELLING

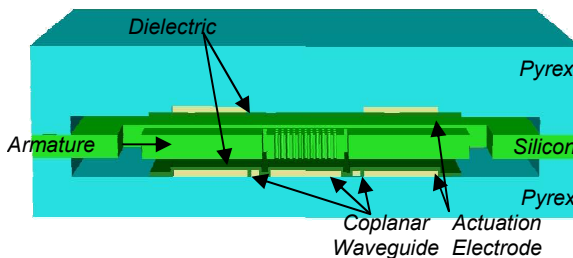


Figure 1: Cross section of the RF MEMS switch.

As shown in Figure 1, there is no mechanical suspension connecting the switch armature to the substrate. The operation of the switch is determined by the application of actuation voltages either at the top or the bottom electrodes. The RF signal travels through the CPW during the up state

or through the armature of switch into the ground planes during the down (shunt) state.

For switching operation to take place, an electrostatic force is defined by eq. 1 and must be greater than the gravitational force acting on the armature. As the armature is a free body, it is electrically floating. In such a configuration, an electrostatic actuation force can only be applied to the armature with at least two actuation electrodes, where each electrode is energised with opposite polarities but equal magnitude voltages [9].

$$F_{electrostatic} = \frac{1}{2} \frac{\epsilon_0 A V_{act}^2}{g_o^2} \quad (1)$$

where ϵ_0 is the permittivity of free space, A is the total area of the actuation electrodes, V_{act} is the applied actuation voltage and g_o is the initial capacitive gap. The minimum actuation voltage can therefore be calculated as:

$$V_{act(min)} \cong \sqrt{\frac{2Gmg_o^2}{\epsilon_0 A}} \quad (2)$$

where m is the mass of the armature, G is the earth gravity.

Effects of Damping Considerations

The small displacement damping coefficient for a pair of parallel plates can be written as [6]:

$$b = \frac{3}{2\pi} \frac{\mu A_{arm}^2}{g_o^3} \quad (3)$$

where μ is the air viscosity and A_{arm} is the area of the armature.

As the damping force for a MEMS switch is dependent on the displacement of the armature, a constant damping coefficient is insufficient to model the behaviour of the armature when in switching mode. In Peroulis [6] case, he derived a displacement compensating damping coefficient equation for modelling larger displacement:

$$b = \frac{k}{\sqrt{\frac{k}{m} Q_o} \left(1 - \left(\frac{g_o - x}{g_o} \right)^2 \right)^{\frac{3}{2}} \left(1 - 9.638 \left(\frac{\lambda}{x} \right)^{1.159} \right)} \quad (4)$$

Where k is the spring constant, Q_o is the nominal small displacement quality factor of the MEMS switch at $x=g_o$ and λ is the mean free path. The last

term in the denominator accounts for slip-flow effect. As there is no mechanical spring in this design, the squeeze film spring constant is substituted and is calculated as given in [10]:

$$k = \frac{64\sigma P_a A}{\pi^8 g_o} \sum_{n_1, n_2 = \text{odd}} \frac{1}{(n_1 n_2)^2 \left((n_1^2 + (n_2 w/l)^2)^2 + \sigma^2 / \pi^4 \right)} \quad (5)$$

where n_1 and n_2 are odd integers, P_a is the atmospheric pressure and σ is the squeeze number. The squeeze number, σ is given by:

$$\sigma = \frac{12 \mu A_{\text{arm}}^2 \omega}{P_a g_o^2} \quad (6)$$

where ω is the frequency of the motion, and can be estimated as $2\pi/\text{period}$. The numerical result for the given design show that the spring force is negligible compared to the inertial and damping forces.

Bao et. al [11] developed a modified Reynold's Equation, where the damping force considers the effects of plates perforated with holes.

$$b = \frac{48\mu}{g_o^3} l^2 (l_m - l)(w_m - l) \quad (7)$$

$$l = \sqrt{\frac{2(g_o - x)^3 (t_a + 0.375\pi r_o^2) \eta}{3\beta^2 r_o^2}} \quad (8)$$

$$\eta = 1 + \frac{3r_o^4 K}{16t_a(g_o - x)^3} \quad (9)$$

where l is the characteristic length, η is a factor for the average damping pressure in a cell caused by air flow and $K = 4\beta^2 - \beta^4 - 4\ln\beta - 3$, where $\beta = r_o/r_c$. The radius of the perforated hole is given by r_o while r_c is the pitch between adjacent holes.

The subsequent simulations use the parameters given in table 1 with the diameter of the perforated hole and the pitch between adjacent holes is assumed to be $5\mu\text{m}$ and $10\mu\text{m}$ respectively.

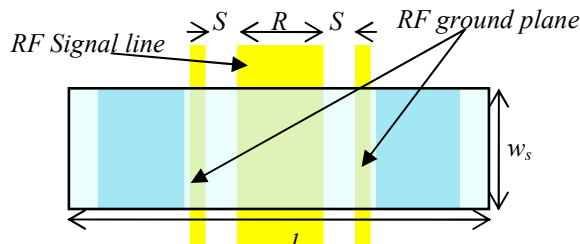


Figure 2: Simplified plan view illustration of the RF MEMS shunt switch.

Table 1: Proposed dimensions of the MEMS switch optimised based on the actuation voltage and switching speed mentioned in [8].

l_s	$680\mu\text{m}$	S	$15\mu\text{m}$
w_s	$80\mu\text{m}$	R	$90\mu\text{m}$
g_o	$5\mu\text{m}$	Armature mass, m	1.84e-9 kg
t_d	$0.2\mu\text{m}$	V_{act}	1.9V

Figure 3 illustrates the Matlab/Simulink simulation results of the switch using the abovementioned

variable and constant damping conditions. The results show that the switch response is slower when variable damping is used. The variable damping effect is able to generate a more reliable result as the damping coefficient of the device is dependent on the displacement of the armature. If the perforated holes are considered, the actuation time is decreased to 14% of the original actuating time that used the solid armature. This result indicates that the effect of the perforated holes cannot be ignored when modelling the MEMS switch.

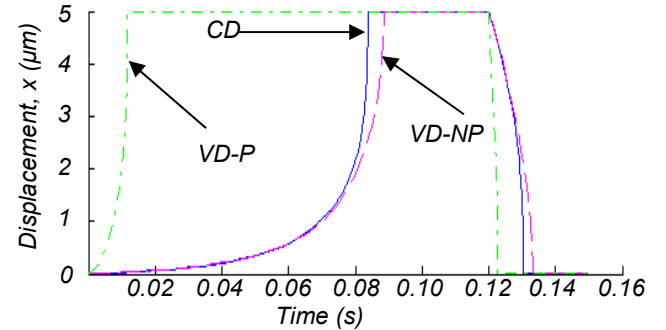


Figure 3: Comparison of actuation time and the release time of the MEMS switch, assuming the model using constant damping (CD), variable damping without considering perforated holes (VD-NP) and variable damping with perforated holes (VD-P).

ELECTROMAGNETIC MODELLING

A conventional RF MEMS shunt switch can be electrically modelled as shown in Figure 4(a). The switching capacitance of the switch can be simply considered as a parallel plate with either an insulating layer only or as an insulating layer and an air gap, as its dielectric layer, depending on the state of the switch. Their values can be calculated as:

$$C_{\text{down}} = \frac{\epsilon_0 \epsilon_r A_t}{t_d} \quad (10)$$

$$C_{\text{up}} = \frac{\epsilon_0 A_t}{g_o + t_d / \epsilon_r} \quad (11)$$

where ϵ_0 is the permittivity of free space, g_o is the initial capacitive air gap, A_t is the area of the armature contacting the transmission line, t_d is the thickness of the dielectric material with dielectric constant, ϵ_r .

However, in the case of the spring-less RF MEMS switch, the armature is not physically attached to

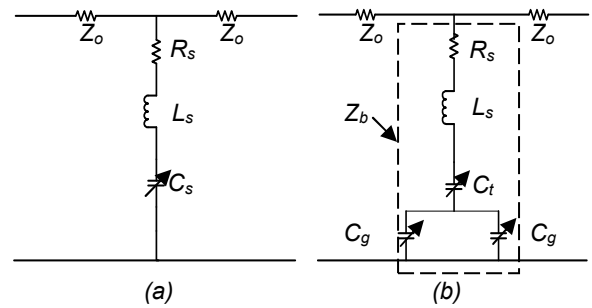


Figure 4: Electrical equivalent circuit of (a) a conventional RF MEMS switch (b) the spring less RF MEMS Switch

any structure. The shunt signal will have to propagate from the CPW signal line to ground plane through i) the air gap between the signal line and armature and ii) the air gap between the armature and ground plane. The formula for the down and up state capacitance needs to be adjusted to account for the additional series capacitive path.

$$C_{down} = \frac{\epsilon_0 \epsilon_r A_t A_g}{t_d (A_t + A_g)} \quad (12)$$

$$C_{up} = \frac{\epsilon_0 A_t A_g}{\left(g_o + \frac{t_d}{\epsilon_r} \right) (A_t + A_g)} \quad (13)$$

where A_g is the area contacting the ground line. This capacitance computation is important as it affects the scattering parameters, which determines the RF performance of the MEMS switch.

The scattering (S) parameters determine the RF performance and characteristics of the switch. The switch can be modelled as a two port network with a shunt network. This will give rise to insertion loss when the switch is in the up state, return loss in both states and the isolation when the switch is actuated. The S_{11} parameter denotes the return loss of the switch in both operating states, while the S_{21} parameter represents the insertion loss and isolation of the switch when in the off and on state respectively. In general, S_{11} and S_{21} can be defined as [12]:

$$S_{11} = -20 \log \left| \frac{-Z_o}{2Z_b + Z_o} \right| \quad (14)$$

$$S_{21} = -20 \log \left| \frac{2Z_b}{2Z_b + Z_o} \right| \quad (15)$$

The return loss is defined as the power reflected over the incident power in a transmission line. In the case of a RF MEMS switch, Z_b is the impedance of the armature. When the armature is not actuated, the resistance and inductance are negligible as the armature does not have any physical contact with the dielectric layer, hence no current passes through the armature. The up state return loss of a capacitive shunt switch can be expressed as:

$$S_{11} \approx -20 \log \left| \frac{-j\omega C_{up} Z_o}{2 + j\omega C_{up} Z_o} \right| \quad (16)$$

where Z_b was substituted according to figure 4(b) and the inductive and resistive terms are neglected, ω is the angular frequency of the RF signal, Z_o is the characteristic impedance of the transmission line and C_{up} is up-state capacitance of the MEMS switch.

The isolation and insertion loss are defined as the transmitted power over the incident power in a transmission line. By substituting the correct armature impedance expression into eq.15 (depending on down or up-state), the isolation or

insertion loss can be defined. Eq. 17-19 is defined as the isolation of the capacitive shunt MEMS switch depending on the frequency of the RF signal.

$$S_{21} \approx \begin{cases} -20 \log \left| \frac{2}{2 + j\omega C_{down} Z_o} \right| & f \ll f_o \\ -20 \log \left| \frac{2R_s}{R_s + Z_o} \right| & f = f_o \\ -20 \log \left| \frac{2j\omega L_s}{2 + j\omega L_s} \right| & f \gg f_o \end{cases} \quad (17)$$

where S_{21} is the magnitude of the isolation and C is capacitance; f_o is the LC series resonating frequency of the switch given by:

$$f_o = \frac{1}{2\pi\sqrt{L_s C_s}} \quad (20)$$

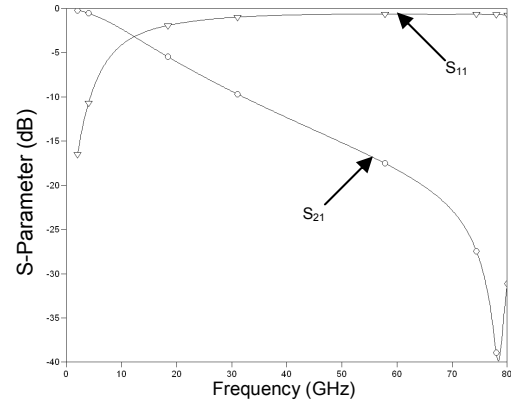


Figure 5: Simulated down state return loss (S_{11}) and isolation (S_{21}) for a 50Ω RF MEMS switch using Sonnet Lite TM.

Figure 5 shows the simulated response of the RF MEMS switch characteristics over a 50Ω CPW transmission line. The EM simulation was implemented from 1-80 GHz using Sonnet Lite. The switch-off resonance frequency is approximately 78GHz with an isolation of 40dB. The switch insertion loss is <0.7 dB at a similar frequency.

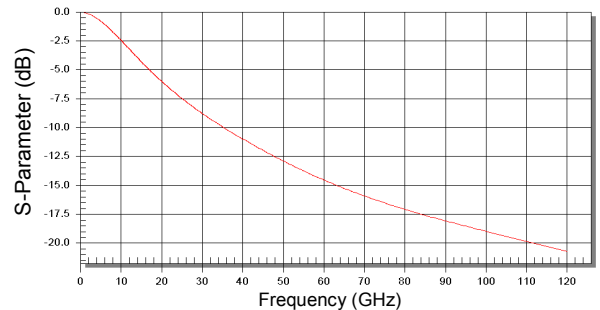


Figure 6: Simulated down state isolation (S_{21}) for a 50Ω RF MEMS switch using Ansoft HFSS

Figure 6 shows the simulated response of the same structure using Ansoft HFSS for a range from 1-120GHz. The simulation shows that the switch has a rejection of more than 16dB when the switch is down and it increases with the frequency of the RF signal. The simulation results of both software tools are comparable for frequencies below 40GHz.

However, for higher frequencies, *SonnetLite*™ decreases rapidly, showing some form of resonance while the HFSS simulation continues to decrease gradually. The difference between the two simulated results at higher frequencies is currently being investigated. This may be due to inductive and capacitive elements in the switch structure.

FABRICATION

The fabrication process requires 9 photolithography steps and will make use of one SOI wafer sandwiched between two Pyrex wafers to form the device. The process can be split into three different parts, mainly Pyrex wafer fabrication, silicon on insulation (SOI) wafer fabrication and assembly of the device.

1. Pyrex Wafer Fabrication

The Pyrex wafers are initially prepared using fuming nitric acid. The top and the bottom Pyrex wafer have a 3 μm cavity trench etched respectively, to create the operating cavity for the armature and provide the space for the bond pads, using Rockwell 7:1 buffered hydrofluoric acid (BHF). A layer of chrome gold (CrAu) is deposited and etched to form the coplanar waveguide, the actuation electrodes and the bond pads of the device. Tantalum pentoxide (Ta_2O_5) is used as the material for the dielectric, which covers the coplanar waveguide and the actuation electrodes. Figure 7 shows the process of the bottom Pyrex wafer. Laser micromachining is subsequently used to create access holes on the top side wafers. These holes act as the windows for the etchant to access the wafer stack during the final release step of the fabrication.

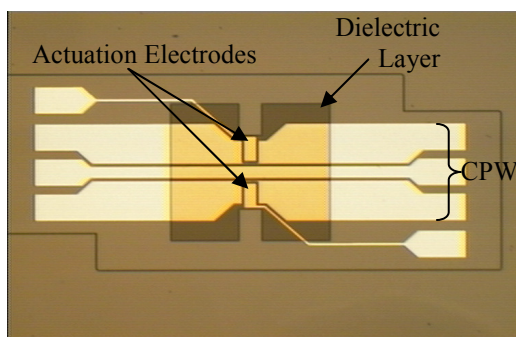


Figure 7: Microscopic picture of structures of a processed bottom Pyrex wafer with a 50Ω CPW.

2. SOI Wafer Fabrication

The armature will be fabricated using SOI wafers. Firstly, a layer of silicon dioxide is deposited using PECVD on the surface of the active layer. This oxide layer is used as a sacrificial layer for the armature. Subsequently, a layer of CrAu is sputtered to form bond pads for the top Pyrex wafer.

3. Device Assembly

The assembly of the device will require the use of anodic bonding twice. The partially processed SOI wafer is firstly anodically bonded to the top Pyrex wafer. This bonding step is required to electrically

connect the metal tracks on the top Pyrex wafer to the bond pads on the SOI wafer. The holding wafer and buried oxide are subsequently removed, exposing the back of the active layer.

The armature is then patterned on the active layer using deep reactive ion etching (DRIE). A second anodic bonding process is employed to attach the bottom Pyrex wafer to the Silicon/Pyrex stack. The wafer can then be diced. The final stage of the fabrication process is to release the armature through an etching process before proceeding to device packaging.

CONCLUSIONS

A Matlab/Simulink model was used to simulate the dynamic response of a novel spring-less MEMS switch. The variable damping model, which accounts for a more realistic damping force with the variation of the capacitive gap, requires a longer switching time when compared to the constant damping effect model. The effect of perforated holes on the damping force cannot be ignored.

The RF characteristic and performance was presented using two EM simulation software tools, both showing good agreement up to 40 GHz. The device is currently being fabricated and prototypes are expected to be available for testing in due course.

ACKNOWLEDGMENT

The author would like to acknowledge the financial support rendered by the Commonwealth Scholarship Commission, U.K.

REFERENCES

1. G. M. Rebeiz *et. al*, *IEEE Microwave Magazine*, 2 (2001), pp 59-71.
2. J. J. Yao, *Journal of Micromechanics and Microengineering*, vol. 10, p. 9, 2000.
3. C. T. C. Nguyen, *et. al*, *Proceedings of the IEEE*, vol. 86, p. 1756, 1998.
4. I. J. Cho, *et. al*, *IEEE Transactions on Microwave Theory and Techniques*, 53 (2005), pp. 2450-57.
5. D. Saisas, *et. al*, *IEEE Journal of Solid-State Circuits*, vol. 38, p. 2318, 2003.
6. D. Peroulis, *et. al*, *Microwave Theory and Techniques, IEEE Transactions on*, vol. 51, pp. 259-270, 2003
7. R. Chan, *et. al*, *J. Microelectromechanical Systems*, vol. 12, pp. 713, 2003
8. K. S. Kiang, *et.al*, *Proc. MME 2006 Conference*, pp. 105-108, UK, Sept. 2006
9. S. J. Woo, *et. al*, *Proceedings of the 34th SICE Annual Conference. International Session Papers*, (1995), pp. 1347-52.
10. J. J. Blech, *J. Lubrication Technology*, vol. 105, pp. 615-620, 1983.
11. M. Bao, *et. al*, *Journal of Micromechanics and Microengineering*, vol. 13, pp. 795-800, 2003.
12. D. M. Pozar, *Microwave Engineering*, 2 ed.: Artech House, 1998.